Rectifying Network Common Items Extraction for Complex Multi-Band Rectifiers: Theory, Design, and Experimental Verification

Yuchao Wang, Zebin Zhu, Shihao Sun, Cheng Zhang, *Member*, *IEEE*, Lei Wang, *Senior Member*, *IEEE*, Ping Lu, *Member*, *IEEE*, and Chaoyun Song, *Senior Member*, *IEEE*

***Abstract*—We present a novel design strategy for complex multiband rectifiers, named the "Rectifying Network Common Items Extraction (RNCIE)". This approach involves sharing one rectifying network (i.e., the common items) between two or more parallel rectifiers, thereby significantly simplifying the design process. In contrast to the traditional global optimization method for multi-band (e.g., >3 bands) rectifier design, our RNCIE strategy can help realize the modular decomposition of the rectifier, including the rectifying network and impedance matching network (with the help of filter branches), thus leading to a significant reduction in design cost and complexity. Additionally, the unique advantage of the RNCIE contributes to in-depth analysis of the influencing factors on the total efficiency of the rectifier. Consequently, the RF-DC conversion efficiency of an example prototype of the rectifier design can be optimized to 44.6% @ 1.8 GHz, 45.4% @ 2.1 GHz, 41.7% @ 2.6 GHz, 33% @ 3.5 GHz, 30.2% @ 4.9 GHz, and 23% @ 5.8 GHz at an input power level of −10 dBm. Meanwhile, our rectifier with a shared rectifying network can improve the total efficiency when multi-tone signal inputs are used (27% @ −20 dBm, 43% @ −10 dBm for a six-tone signal). The strategy is verified by experimental measurements and paves the way for the efficient and accurate design of multi-band rectifiers of high efficiency.**

***Index Terms*—Energy harvesting, high efficiency rectifiers, multi-band rectifiers, simplified rectifying network.**

I. Introduction

With the rapid development of fifth-generation (5G) wireless communication technology, our lives are gradually moving from the Internet of Things (IoTs) proposed in 1999 [1–3] to the Internet of Everything (IoE) [4]; consequently, numerous sensors are being adopted in all aspects of our daily life for external stimuli detection. Therefore, to power them for long-term stability is an important issue. It is an enormous challenge to replace the depleted batteries to continue their service time. To address this problem, harvesting energy (such as wind [5], solar [6], kinetic [7], and radio frequency (RF) energy [8–10]) from the surrounding environment to power low-power devices is gaining increased attention. Compared with wind, solar, and kinetic energy, RF energy, even at low ambient power levels, is a potential candidate because of its all-weather usage advantage [11–13], as well as its ubiquitous presence over a wide frequency range resulting from the extensive distribution of RF sources, such as communication base stations, wireless Bluetooth devices, and Wi-Fi routers [14–16].

Rectennas are powerful tools that can capture surrounding RF signals and convert them into DC power [17–19]. To facilitate practical applications of rectennas, the receiving antenna should be able to gather RF signals from as many frequency bands as possible [20–22], while considering their actual ambient power level. Hence, the corresponding rectifier must be able to efficiently handle the received multi-band RF power, which is challenging owing to the nonlinear nature of diodes [23–26].

Significant efforts have been made to design multi-band rectifiers [27–30]. Various design architectures have been proposed to enhance the working performance, including single RF chain with DC combining [31–33] and multiple RF chains with DC combining [34–37]. Regarding the single RF chain design architecture, the total RF-DC conversion efficiency is always slightly low and difficult to be improved because of the relatively high insertion loss of the complex matching network required for multiple bands. For example, a quad-band rectifier based on the single RF chain design architecture was proposed in [31]. However, its RF-DC conversion efficiency was only 12% @ 0.9 GHz, 18% @ 1.8 GHz, 10% @ 2.45 GHz, and 5% @ 5.8 GHz at an input power of –10 dBm. To improve the RF-DC conversion efficiency, a matching network elimination technology based single RF chain was presented in [32], which enables tuning of the antenna impedance to a required value equal to the direct complex conjugate match with the rectifier impedance. Through deliberate design, the efficiency of the proposed rectifier can reach 65% @ 1.46 GHz, 60% @ 1.85 GHz, 62% @ 2.15 GHz, and 52% @ 2.5 GHz when the input

This work was supported in part by the National Natural Science Foundation of China (62101394), the Fundamental Research Funds for the Central Universities (WUT: 2021IVA064, and 2021IVB029), Beijing Nova Program (2304842874), and the Foundation from the Guangxi Key Laboratory of Optoelectronic Information Processing (GD21203). (*Corresponding authors: Cheng Zhang; Chaoyun Song*)

Y. Wang, Z. Zhu, S. Sun, and C. Zhang are with Shanghai Institute of Optics and Fine Mechanics, Chinese Academy of Sciences, Shanghai, 201800, China, and are also with Hangzhou Institute for Advanced Study, University of Chinese Academy of Sciences, Hangzhou, 310024, China. (e-mail: yuchao9629@whut.edu.cn; ze1704@whut.edu.cn; 272960@whut.edu.cn; czhang2020@whut.edu.cn).

L. Wang is with the School of Engineering and Physical Sciences, Institute of Sensors, Signals and Systems, Heriot-Watt University, EH14 4AS, United Kingdom. (e-mail: lei.wang@hw.ac.uk).

P. Lu is with the School of Electronics and Information Engineering, Sichuan University, Chengdu, 610064, China. (e-mail: pinglu90@scu.edu.cn).

C. Song is with the State Key Laboratory of Radio Frequency Heterogeneous Integration, Shenzhen University, Shenzhen, 518060, China, and is also with the Department of Engineering, King's College London, London, WC2R 2LS, UK. (e-mail: chaoyun.song@kcl.ac.uk).

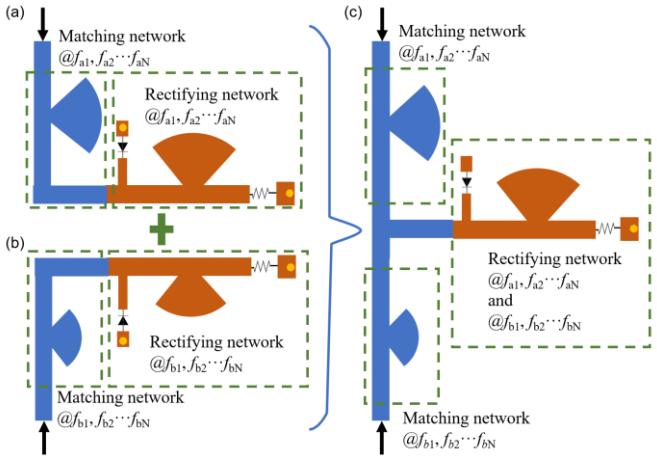

Fig. 1. Design process of the proposed rectifier using the RNCIE strategy.

power is set to 0 dBm. However, the designed eliminating matching network seriously limits the flexibility of the rectifier and receiving antenna design.

To enhance the RF-DC conversion efficiency, a multiple RF chains architecture was built, wherein discrete rectifier branches were connected in parallel and operated at limited frequencies. Owing to the relatively simple matching network, the matching efficiency and insertion loss can be optimized, thus resulting in an improvement in the total efficiency. For example, in [34], a six-band rectifier was designed using the multiple RF chains strategy. Their proposed rectifier demonstrated high simulated RF-DC conversion efficiency at the target frequencies (60% @ 0.55 GHz, 55% @ 0.75 GHz, 61% @ 0.9 GHz, 52% @ 1.85 GHz, 45% @ 2.15 GHz, and 36% @ 2.45 GHz), while working only at five frequency bands with the significantly decayed efficiency (47% @ 0.55 GHz, 42% @ 0.75 GHz, 51% @ 0.9 GHz, 35% @ 1.85 GHz, and 37% @ 2.3 GHz) at an input power level of −10 dBm. This was attributable to the uncertain parasitic behavior of the surface mount technology (SMD) components used in the circuit. Subsequently, in [35], a seven-band rectifier was designed using microstrip lines instead of SMD components to match the impedance. With the improved impedance matching technique, the measured results agreed well with the simulated ones, and the rectifier demonstrated high RF-DC conversion efficiency at −10 dBm (44.4% @ 1.84 GHz, 43.9% @ 2.04 GHz, 45.4% @ 2.36 GHz, 43.4% @ 2.54 GHz, 36.1% @ 3.3 GHz, 32.4% @ 4.76 GHz, and 28.3% @ 5.8 GHz). However, a problem exists in the multiple RF chains based rectifier design: each RF chain is highly correlated with the other branches within the multiple RF chains structure, and thus, designing one of them independently without considering the others is challenging through the existing approaches. The general approach for addressing this problem is global optimization, which involves a complex parameter scanning process and is time-consuming. Therefore, a new design strategy is urgently needed to improve the existing situation and facilitate the efficient and accurate design of a multi-band rectifier.

Herein, a novel design strategy, named the "Rectifying Network Common Items Extraction (RNCIE)", was proposed to address the aforementioned problems. In our design

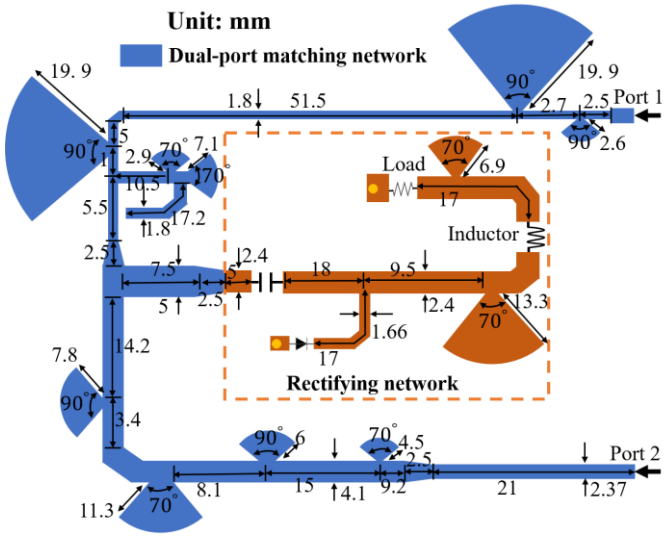

Fig. 2. Topology of the proposed three-port rectifier using the RNCIE strategy and three-port impedance matching network.

architecture shown in Fig. 1, the rectifying networks (i.e., the common items) are extracted from two parallel rectifiers (one for f_{a1}, f_{a2}, …, f_{aN} in Fig. 1(a) and the other for f_{b1}, f_{b2}, …, f_{bN} in Fig. 1(b)) and shared by two different matching networks (Fig. 1(c)). Two filter branches were predesigned to fix the dual-port input impedance and overcome the mutual coupling between the two matching networks. Thus, the impedance transformation branches before the filter branches can be easily obtained owing to the clarity of the impedance of the filter branches. With the help of the RNCIE design strategy, the rectifying and matching networks of flexible operating frequencies can be designed independently without conducting global optimization, catering to the aim for efficient and accurate design of the multi-band rectifier. Through our design method, a dual-port six-band rectifier has been achieved with high RF-DC conversion efficiency at the preset six frequency bands (43.3% @ 1.8 GHz, 43.5% @ 2.1 GHz, 40.8% @ 2.6 GHz, 32% @ 3.5 GHz, 30% @ 4.9 GHz, and 21% @ 5.8 GHz at –10 dBm). Additionally, considering the one diode shared feature of our design, the multi-tone input signal can help enhance the total RF-DC conversion efficiency (18.7% @ 1.8 GHz + 5.8 GHz, 17.2% @ 2.1 GHz + 4.9 GHz, and 20% @ 2.6 GHz + 3.5 GHz at −20 dBm), which also has been proved by simulations and measurements. The rest of this paper is organized as follows. The design process of the rectifying network is introduced in Section II. A three-port matching network design is presented in Section III. A performance evaluation of the proposed rectifier is presented in Section IV. Finally, conclusions are drawn in Section V.

II. Rectifying Network Design

Before designing the rectifier, its operation frequencies were preset as 1.8 GHz, 2.1 GHz, 2.6 GHz, 3.5 GHz, 4.9 GHz, and 5.8 GHz, covering the common commercial GSM1800, LTE, Wi-Fi/WLAN, and 5G bands, for improving its versatility. Unlike the traditional design method of global optimization, the rectifying and matching networks of our rectifier are designed

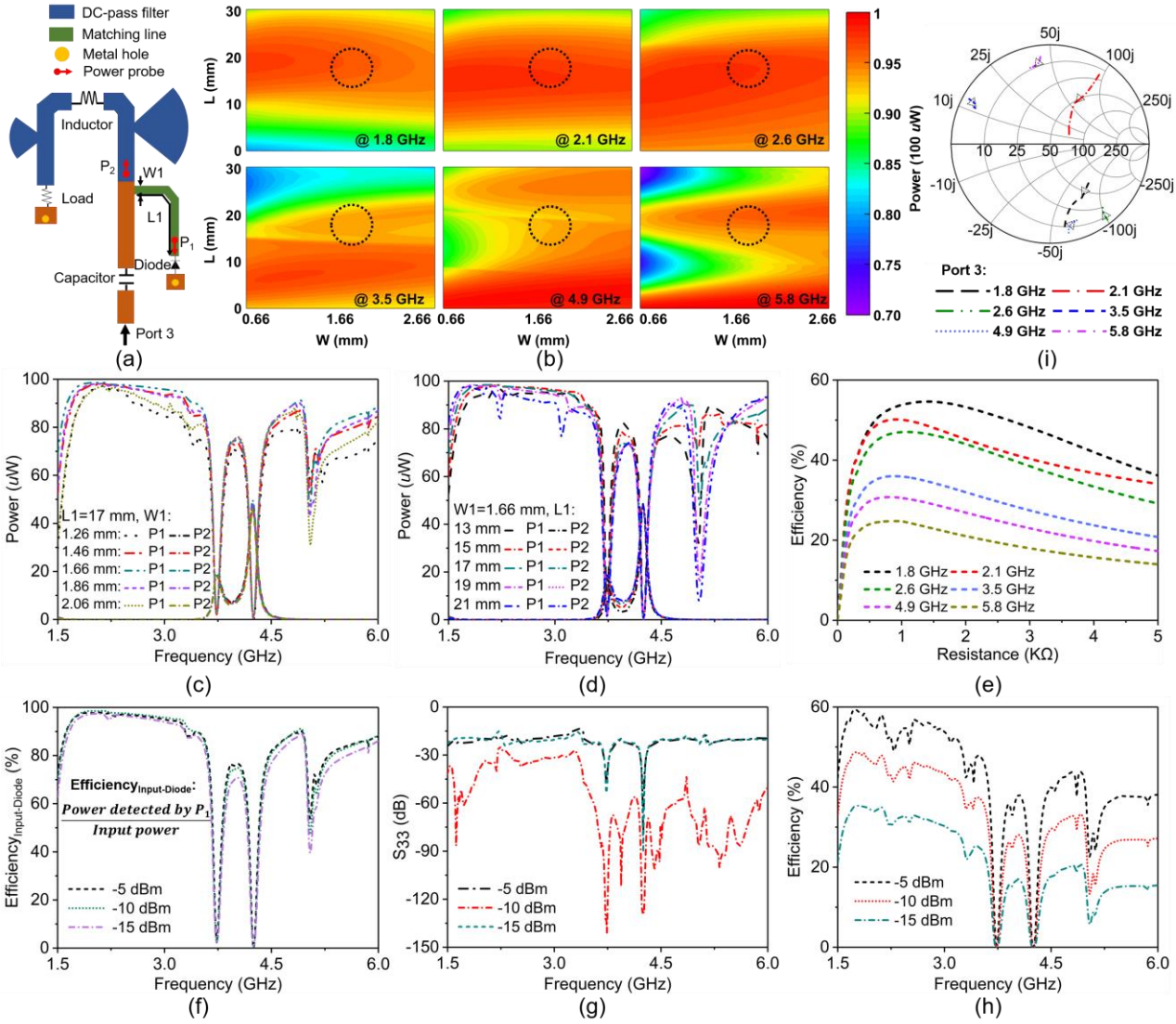

Fig. 3. (a) Topology of the proposed rectifying network. (b) Simulated power detected by P1 versus W1 and L1 at six frequencies as the rectifying network is ideally matched. Simulated power detected by P1 and P2 of the proposed rectifying network with different values of (c) W1 and (d) L1 as the rectifying network is ideally matched. (e) Simulated RF-DC efficiency of the rectifying network as a function of load resistance at six frequencies. (f) Simulated $\text{Efficiency}_{\text{Input-Diode}}$ at different input powers as the rectifying network is ideally matched. (g) Simulated reflection coefficient of the proposed rectifier network at different input power levels when the port impedance is set to match the input impedance of the rectifier conjugately over the frequency band of interest. (h) Simulated RF-DC conversion efficiency of the proposed rectifying network at different input power levels (for ideal matching case). (i) Input impedance of port 3 as a function of input power (varying along the arrow from –25 dBm to 5 dBm) at six frequencies. The load is fixed to 900 Ω.

independently to gain insight into their working principles and maximize RF-DC conversion efficiency.

To obtain the matching impedance of the three-port matching network following designed, a rectifying network was first proposed to efficiently convert RF energy into DC power. It consists of a diode, a matching line (green parts), a DC-pass filter (blue parts and inductor (22 nH)), a blocking capacitor (10 pF), and a load, as shown in Fig. 3(a). The Schottky diode SMS7630 was chosen as the rectifier diode because of its low bias voltage at low power input levels (forward bias voltage: 60–120 mV at 0.1 mA) [38] and low loss. Subsequently, a six-band DC-pass filter composed of an inductor and two radial stubs (blue part in Fig. 3(a)) was designed based on the selected diode to prevent the leakage of the input RF power and enhance the RF-DC conversion efficiency. Within the DC-pass filter, the inductor was chosen to prevent low-frequency (1.8 GHz, 2.1 GHz, and 2.6 GHz) energy from flowing through the load, and the two radial stubs had the same functionality at high frequencies (3.5 GHz, 4.9 GHz, and 5.8 GHz). Using a DC-pass filter, the input RF power can be confined to a rectifying network without ground leakage. However, not all of the RF power that enters the rectifying network flows into the diode and is converted into DC energy, owing to the resonant loss of the circuit. Only the diode can perform RF-DC rectification owing to its nonlinear characteristics.

To maximize the RF power into the diode, the matching line must be optimized. Before the optimization process, two power probes (P1 and P2) were used to monitor the RF power flowing into the diode and DC-pass filter, respectively, as the input power from port 3 was fixed to –10 dBm (100 *u*W), as shown in Fig. 3(a). Subsequently, to demonstrate the combined influence

of W1 and L1 on the power directed to the diode, we depict the power variations entering the diode in relation to both L1 and W1 across six frequencies, as illustrated in Fig. 3(b). While it's evident that both W1 and L1 influence the power, pinpointing their optimal values from Fig. 3(b) is challenging. As a remedy, we identified a zone where the power showcased optimal values across the six frequencies, as shown in Fig. 3(b). Subsequently, leveraging this region as a reference, we executed one-dimensional analyses for W1 and L1 individually to determine the optimal parameters. Next, the width (W1) and length (L1) of the matching line were independently analyzed to improve the amount of RF energy entering the diode. Evidently from Figs. 3(c) and 3(d), regardless of the parameter changes, the RF power detected by P2 barely varied and was virtually zero in the preset bands, thus demonstrating the good RF isolation performance of the predesigned DC-pass filter. The RF power detected by P1 is shown in Figs. 3(c) and 3(d). As shown in Fig. 3(c), the RF power (for all preset frequencies) flowing into the diode reached its maximum value when W1 was 1.66 mm, whereas the power detected by P1 exhibited great sensitivity to changes in L1 (Fig. 3(d)). With the increase in L1 (Fig. 3(d)), the RF power entering the diode deteriorated at low frequencies (2.6 GHz and 3.5 GHz) and improved at a high frequency of 5.8 GHz. Finally, by balancing the six-band performance, L1 was set to 17 mm. In fact, along with the above analysis, we also performed a simultaneous optimization of the load resistance to determine the best RF-DC conversion performance of the rectifying network. However, due to the enormous amount of the data appearing during the global optimization, we only adopt the optimized load resistance – 900 Ω to exhibit the design flow (Figs. 3(b-d)). Then to reveal the impact of load resistance on the efficiency of the rectifying network, the RF-DC efficiency is provided in Fig. 3(e) as a function of the load resistance at six different frequencies with an input power level of −10 dBm. It is evident that the maximum efficiency corresponds to a load resistance of roughly 900 Ω for the frequencies respectively of 3.5 GHz, 4.9 GHz, and 5.8 GHz. In the meantime, 900 Ω also can support the robust conversion efficiency at higher frequencies.

Once the rectifying network was finalized, the features of the established rectifying networks will be discussed in the following part. Before evaluating the reflection coefficient and RF-DC conversion efficiency of the rectifying network, the effective RF power into the diode was investigated to demonstrate the high RF energy utilization of our design. In Fig. 3(f), the ratio of the energy entering the diode to the input RF power ($\text{Efficiency}_{\text{Input-Diode}}$) was calculated as a function of the frequency at different input power levels. Notably, the $\text{Efficiency}_{\text{Input-Diode}}$ over the entire range of operation frequencies was more than 88% and always maintained stability at input power levels of −5 dBm, −10 dBm, and −15 dBm, thus reflecting that our design has great potential in boosting the RF-DC conversion efficiency once the intrinsic efficiency of the diode is improved to a higher level.

Next, to evaluate the RF-DC conversion efficiency of our design at different input power levels, the port impedance of port 3 under input powers of −5 dBm, −10 dBm, and −15 dBm

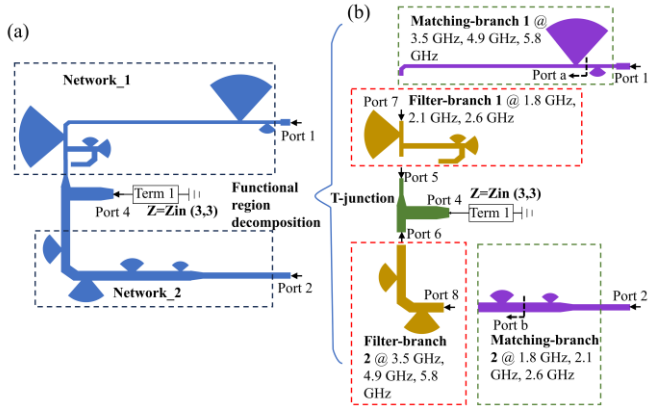

Fig. 4. (a) Topology of the proposed three-port matching network and (b) its functional region decomposition.

was set to match the input impedance of the rectifying network conjugately as a function of frequency when the load was fixed to 900 Ω to ensure that most of the input power enters the rectifying network. The corresponding reflection coefficient of the proposed rectifier network is shown in Fig. 3(g), and the ultra-low S_{33} denotes that most of the RF energy can flow into the rectifying network at input power levels of −5 dBm, −10 dBm, and −15 dBm. The simulated RF-DC conversion efficiency of the proposed rectifying network at different input power levels is also provided in Fig. 3(h). Evidently, the designed rectifying network achieved relatively high conversion efficiency at the six working bands even at different input powers (including −15 dBm, −10 dBm, −5 dBm). Joint consideration of Fig. 3(g) and Fig. 3(h), the RF-DC conversion efficiency of the diode is directly proportional to the RF power flowing into it, up to its penetration power, in accordance with its nonlinear characteristics. Finally, to guide the subsequent design of the matching network, the input impedance of the rectifying network as a function of the input power at six frequency bands was obtained using ADS software. This information is presented in Fig. 3(i).

III. Three-port Matching Network Design

The three-port matching network (Fig. 4(a)) is the final component of the dual-port rectifier connected to the back-end rectifying network. The matching performance ultimately determines the total RF-DC conversion efficiency of the entire device. To realize the one-diode-shared multi-band rectifier, a three-port matching network, as shown in Fig. 4(a) is necessary to be deliberately designed. The traditional way of designing a multi-port matching network involves performing global optimization [34–36], in which the functional zones (e.g., matching branch and filter branch) are mixed together, thus rendering difficulty in analyzing the factors influencing matching efficiency. In addition, even when one of the port input impedances is fixed, as in our designed T-junction (green part in Fig. 4(b)), the other two ports are still mutually coupled, and their input impedances are interdependent. This presents a significant design challenge and requires considerable time for optimization. To address these problems, we introduced a novel design strategy for the required matching network. For a typical

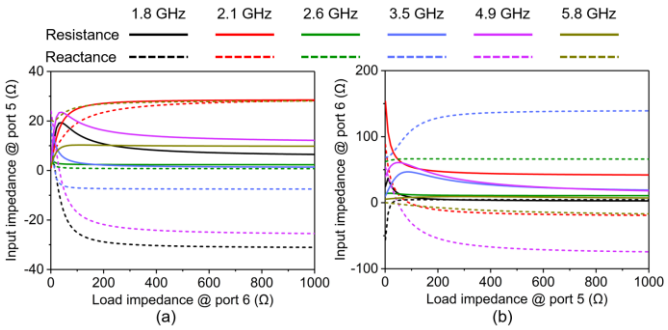

Fig. 5. (a) Simulated input impedance for port 5 when the load impedance of port 6 varies from 1 Ω to 1000 Ω. (b) Simulated input impedance for port 6 when the load impedance of port 5 varies from 1 Ω to 1000 Ω.

three-port network, as shown in Fig. 4(a), the corresponding S-matrix can be expressed as follows [39].

$$S = \begin{pmatrix} S_{11} & S_{12} & S_{14} \\ S_{21} & S_{22} & S_{24} \\ S_{41} & S_{42} & S_{44} \end{pmatrix}. \quad (1)$$

Note that the primary objective of the three-port network is to guide the input signals with frequencies of 3.5 GHz, 4.9 GHz, and 5.8 GHz from port 1 to port 4 without any loss, and signals with frequencies of 1.8 GHz, 2.1 GHz, and 2.6 GHz from port 2 to port 4. Considering the reciprocal nature of the network, S_{14} parameter must be equal to S_{41}. Therefore, the corresponding S matrix in (1) can be rewritten as:

$$S = \begin{pmatrix} S_{11} & S_{12} & 1 \\ S_{12} & S_{22} & S_{24} \\ 1 & S_{24} & S_{44} \end{pmatrix}. \quad (2)$$

This lossless network must satisfy the following conditions [39].

$$S_{11}^{*}S_{12} + S_{12}^{*}S_{22} + S_{24} = 0, \quad (3)$$

$$S_{12}^{*} + S_{22}^{*}S_{24} + S_{24}^{*}S_{44} = 0, \quad (4)$$

$$S_{11} + S_{24}^{*}S_{12} + S_{44}^{*} = 0, \quad (5)$$

$$|S_{11}|^2 + |S_{12}|^2 + 1 = 1, \quad (6)$$

$$|S_{12}|^2 + |S_{22}|^2 + |S_{24}|^2 = 1, \quad (7)$$

$$1 + |S_{24}|^2 + |S_{44}|^2 = 1. \quad (8)$$

Subsequently, $S_{12} = 0$ and $S_{11} = 0$ as the design condition can be derived from (3)-(8). That's to say, a band-stop filter for 1.8 GHz, 2.1 GHz, and 2.6 GHz must be built in Network_2 to achieve the required isolation and satisfy $S_{11} = 0$, and a corresponding matching network is needed in Network_1. Thus, the boundary condition for the unidirectional transmission of the signals (3.5 GHz, 4.9 GHz, and 5.8 GHz) from port 2 to port 4, can also be revealed as $S_{21} = 0$ and $S_{22} = 0$ via the similar calculation method as mentioned above. Consequently, a band-stop filter for 3.5 GHz, 4.9 GHz, and 5.8 GHz in Network_1 while a matching network for these identical frequencies in Network_2 is simultaneously needed to realize the desired transmission performance.

According to the abovementioned design boundary conditions, two filter branches (termed as Filter-branch 1 and

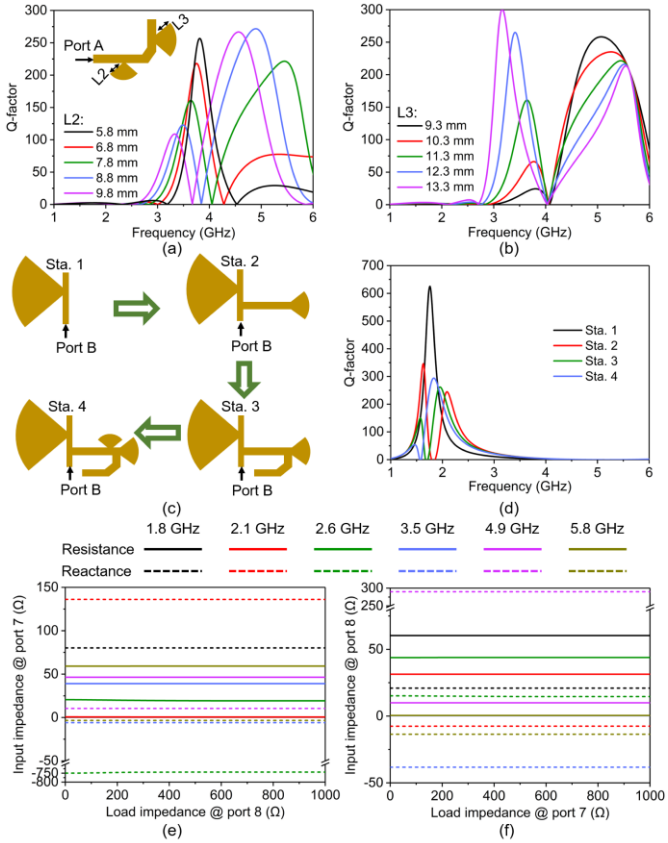

Fig. 6. Simulated Q-factor of the Filter-branch 2 as a function of frequency with different values of L2 (a), and L3 (b). (c) Design process of the Filter-branch 1. (d) Simulated Q-factor of Filter-branch 1 as a function of frequency in the design process. (e) Simulated input impedance for port 7 when the load impedance of port 8 varies from 1 Ω to 1000 Ω. (f) Simulated input impedance for port 8 when the load impedance of port 7 varies from 1 Ω to 1000 Ω.

Filter-branch 2, yellow parts in Fig. 4(b)) in our matching network were first designed to isolate the input impedances of ports 7 and 8 (Fig. 4(b)). These two filter branches can smoothly make the functional sections of the matching network modular, as shown in Fig. 4(b), thus facilitating its performance analysis and rapid design.

Before designing the Filter-branch 1 and Filter-branch 2, a T-junction (green part in Fig. 4(b)) is required to link port 1 (for 3.5 GHz, 4.9 GHz, and 5.8 GHz) and port 2 (for 1.8 GHz, 2.1 GHz, and 2.6 GHz) with port 3. Regarding the designed T-junction, term 1 is connected to its port 4 to ensure that the load impedance of port 4 is identical to the input impedance of the rectifying network (Zin (3, 3) at the input level of −10 dBm), as shown in Fig. 4(b). Similar to the traditional three-port network, as shown in Figs. 5(a), when the load impedance of port 6 varies from 1 Ω to 1000 Ω, the input impedance at port 5 exhibits significant fluctuations in resistance and reactance within the preset frequency bands. Moreover, a similar phenomenon can be observed in Figs. 5(b). The altered impedance of port 5 can induce severe fluctuations in the input impedance of port 6, which is a serious obstacle in designing a three-port matching network.

To stabilize the port impedance, we introduced two band-stop filter branches (yellow parts in Fig. 4(b)) connected to port 5 and port 6 to improve the isolation between port 7 and

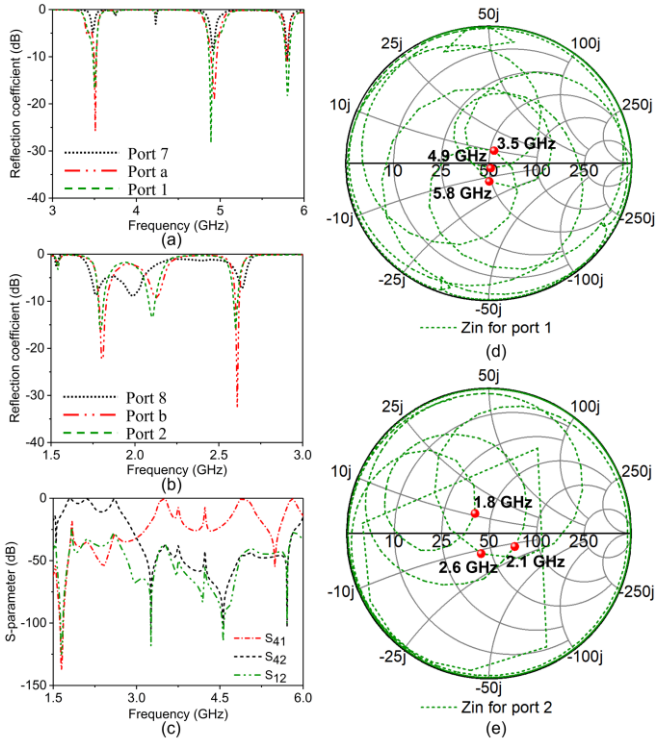

Fig. 7. (a) Simulated reflection coefficient for port 7, port a, and port 1. (b) Simulated reflection coefficient for port 8, port b, and port 2. (c) Simulated S-parameter of the proposed three-port matching network for S_{41}, S_{42} and S_{12}. Real and imaginary part of the input impedance for: (d) port 1 and (e) port 2.

port 8 (the input ports of the two band-stop filter branches in Fig. 4(b)). Filter-branch 1 is designed for 1.8 GHz, 2.1 GHz, and 2.6 GHz, whereas Filter-branch 2 is designed for 3.5 GHz, 4.9 GHz, and 5.8 GHz. When it comes to band-stop filters, there are primarily two methodologies: reflection-type and absorption-type. For absorption-type band-stop filters, RF energy within a designated frequency range enters the filter via one port but gets dissipated within the structure, preventing its passage through the other port. On the other hand, reflection-type band-stop filters repel RF signals by reflecting the energy within the stopband back to its source. Our design emphasizes the use of reflection-type filters, primarily due to their ability to conserve energy. It is crucial to underscore that, in our particular design, assessing the band-stop filter's performance can't be rooted in the transmission coefficient due to the absence of pertinent port impedance data. However, as highlighted in previous research [40-41], reflection-type filters boast a high-quality factor (Q-factor). With this in mind, our initial filter branch design was tailored to achieve a high Q-factor within our target frequency band.

Firstly, Filter-branch 2 is designed, which consists in two radial stubs, as shown in Fig. 6(a). To investigate the influence of the radial stub's length on the operational frequency, the Q-factor as a function of frequency with varying values of L2 and L3 is depicted in Figs. 6(a-b). It is evident from Fig. 6(a) that as L2 increases, the second peak shifts to lower frequencies. While the first peak also shifts to lower frequencies, this phenomenon can be attributed to the impact of L2 on the frequency at which the Q-factor reaches zero. Furthermore, Fig. 6(b) reveals that with an increase in L3, the frequency corresponding to the first peak shifts to lower frequencies. To achieve a high Q-factor at 3.5 GHz, 4.9 GHz, and 5.8 GHz, 7.8 mm and 11.3 mm are chosen as the values of L2 and L3, respectively.

Subsequently, we designed Filter-branch 1 for the 1.8 GHz, 2.1 GHz, and 2.6 GHz. This design comprises a radial stub and an additional parallel branch. Given the proximity of its operating frequencies, a broadband band-stop filter is ideal for Filter-branch 1. Initially, a radial stub, showcased as sta. 1 in Fig. 6(c), was added to the transmission line, targeting a high Q-factor at 1.8 GHz, as depicted in Fig. 6(d). To achieve a high Q-factor at 2.1 GHz, an additional segment of transmission line combined with a radial stub was introduced, represented as sta. 2 in Fig. 6(c). This integration, however, induced a zero Q-factor node at 1.8 GHz. To optimize performance, both a radial stub and an open stub were designed, referenced as sta. 3 and sta. 4 in Fig. 6(c). These aimed to shift the frequency corresponding to the zero Q-factor node to a lower value. Consequently, Filter-branch 1 achieves high Q-factor surpassing 40 within the 1.8 GHz to 2.6 GHz. With this, the design of the two Filter-branches was completed.

To further evaluate the performance of the two band-stop filter branches, the input impedance of port 7 as a function of load impedance of port 8 is shown in Fig. 6(e). Evidently, the resistance and reactance of the input impedance for port 7 always maintained stability, even when the load impedance varies from 1 Ω to 1000 Ω. Regarding to Filter-branch 2, when changing the load impedance of port 7, the stable input impedance of port 8 can be observed as desired (Fig. 6(f)), as well as the band-stop feature at 3.5 GHz, 4.9 GHz, and 5.8 GHz.

Based on these two predesigned filter branches, the input impedance of port 7 and port 8 can be obtained by using ADS software. Next, the matching network needs to be implemented to adjust the input impedance of the port 7 and port 8 to standard 50 Ω. In the realm of matching network design, our approach initially began with a single frequency band. As our exploration progressed, we discovered that the frequency dependence of the matching remained notably robust across our target power range. This insight led us to develop two separate matching networks: Matching-branch 1 and Matching-branch 2. To ensure optimal matching performance across a wide power range (−15 dBm to −5 dBm), we used an intermediate power level of −10 dBm as our benchmark for designing the matching network. Next, the reflection coefficient of port 7 is provided in Fig. 7(a). It is obvious that the resonance occurs at 5.8 GHz despite the absence of a matching branch. Furthermore, the Matching-branch 1 consisting of two cascaded T-type matching networks is employed to match the input impedance to 50 Ω at 3.5 GHz and 4.9 GHz. It is worth noting that there is an infinite number of potential solutions when designing a matching network for a frequency using a T-type matching network. This means the reflection coefficient at 5.8 GHz can be further optimized. Subsequently, a T-type matching network (between port 7 and port a in Fig. 4(b)) is introduced to shift the input impedance for 3.5 GHz, with the reflection coefficient depicted in Fig. 7(a). Moreover, another T-type matching network

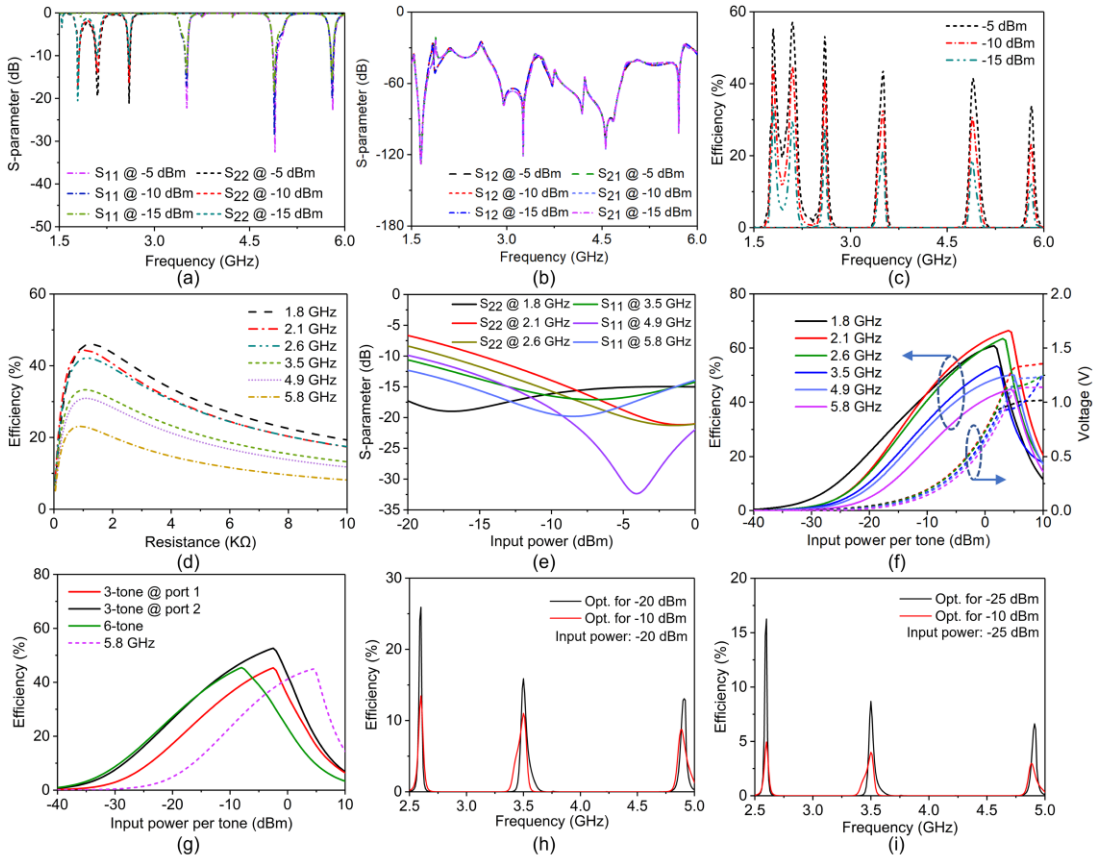

Fig. 8. (a) Simulated reflection coefficient, (b) S_{12}, S_{21}, and (c) RF-DC conversion efficiency of the proposed rectifier at different input power levels. (d) Simulated RF-DC conversion efficiency of the proposed rectifier versus load resistance at six bands with an input power of −10 dBm. (e) Simulated S-parameter as a function of input power for six frequencies. (f) Simulated RF-DC conversion efficiency and output voltage of the proposed rectifier versus input power level at six frequencies. (g) Simulated RF-DC conversion efficiency of the proposed rectifier versus input power level for single- and multi-tone input signals. The load resistance is 900 Ω. Simulated RF-DC efficiency with the input power level of -20 dBm (h), and -25 dBm (i) as the rectifier is optimized for different power levels.

(positioned between port a and port 1 in Fig. 4(b)) is utilized to adjust the frequency corresponding to the second resonance to 4.9 GHz, as illustrated in Fig. 7(a).

Similar to Matching-branch 1, Matching-branch 2 is also composed of two T-type matching networks. With the help of the first T-type matching network (between port 8 and port b in Fig. 4(b)), the first two resonances move towards higher frequencies and the third resonance peak moves towards lower frequency, and the frequencies corresponding to the first and third resonance were tuned to 1.8 GHz and 2.6 GHz, as shown in Fig. 7(b). Immediately after that, the frequency corresponding to the second resonance is tuned to 2.1 GHz by designing the second T-type matching network (between port b and port 2 in Fig. 4(b)).

All components of the matching network were completed according to the previously proposed design principle. To evaluate the matching performance of the proposed three-port matching network, the simulated S_{12} (denoting the RF power from port 2 to port 1) of the matching network is shown in Fig. 7(c) to determine the isolation performance between ports 1 and 2. It can be seen that S_{12} was less than –15 dB at the target frequency bands, thus indicating the ultra-low crosstalk between these two ports. Although the isolation and reflection coefficients of the two ports have been studied, the matching efficiency of the matching network remains an essential evaluation criterion owing to its impact on the overall RF-DC efficiency of the rectifier. Therefore, S_{41} and S_{42} of the proposed matching network were simulated, and the corresponding data are shown in Fig. 7(c). The corresponding data (−0.28 dB @ 1.8 GHz, −0.42 dB @ 2.1 GHz, −0.42 dB @ 2.6 GHz, −0.39 dB @ 3.5 GHz, −0.29 dB @ 4.9 GHz, and −0.42 dB @ 5.8 GHz) were all more than –0.5 dB at the designed six bands, thus indicating good transmission efficiency and small insertion loss of the optimized three-port matching network, which further proves the correctness of the design method. Additionally, the input impedances of ports 1 and 2 as a function of frequency are shown in Figs. 7(d) and 7(e), which favors the frontends design. Despite the proposed structure (Fig. 2) being slightly complex and relatively large size, each part of the rectifier is considerably easier to construct compared to traditional design strategies. This offers a time and resource-saving solution. Furthermore, the separate components within our rectifier can be optimized individually to achieve optimal performance. In the meantime, we believe that it is possible to achieve a smaller-sized rectifier by incorporating surface-mounted components instead of microstrip lines, as demonstrated in [34].

IV. Performance Evaluation of the Dual-Port Six-Band Rectifier

To evaluate the overall performance of the proposed rectifier, port 3 was connected to port 4 (the detailed structural parameters are shown in Fig. 2). The final simulated reflection coefficient of the optimized six-band rectifier at three input power levels of −5 dBm, −10 dBm, and −15 dBm is shown in Fig. 8(a). The results indicate that the proposed rectifier has excellent matching performance, as evidenced by the fact that both S_{11} and S_{22} values are below −10 dB. To observe the isolation between ports 1 and 2, the simulated S_{12} of the proposed rectifier at different input power levels is supplied in Fig. 8(b). The results show that S_{12} is below −20 dB, thus indicating that the two ports have a low coupling advantage. Next, to evaluate the overall RF-DC efficiency of the proposed rectifier at different input power levels, the simulated RF-DC conversion efficiency as a function of the frequency is shown in Fig. 8(c). Evidently, when the input power was −10 dBm, the efficiency of the proposed rectifier achieved 44.6% @ 1.8 GHz, 45.4% @ 2.1 GHz, 41.7% @ 2.6 GHz, 33% @ 3.5 GHz, 30.2% @ 4.9 GHz, and 23% @ 5.8 GHz, respectively. In addition, at the same power level, the efficiency at lower frequencies (1.8 GHz, 2.1 GHz, and 2.6 GHz) was higher than the efficiency at higher frequencies (3.5 GHz, 4.9 GHz, and 5.8 GHz) owing to the higher loss of diode and the dielectric substrate at higher frequencies. To investigate the effect of load resistance on RF-DC efficiency, Fig. 8(d) shows the simulated results of RF-DC conversion efficiency versus load resistance for the proposed rectifier in the six frequency bands at an input power of −10 dBm. As the load resistance increased, the efficiency first increased and then decreased, and the RF-DC conversion efficiency reached a maximum at 900 Ω for 3.5 GHz, 4.9 GHz, and 5.8 GHz. Therefore, 900 Ω was chosen as the load resistance of the rectifier to balance the RF-DC conversion efficiency at the six operation frequency bands. Additionally, the conversion efficiency remained relatively high for overload resistances ranging from 500 to 5000 Ω.

In addition, the impact of the input power level on the reflection coefficient of the six frequencies was analyzed and is plotted in Fig. 8(e). It can be seen from Fig. 8(e) that the rectifier is well matched with standard 50 Ω over the power range of –15 dBm ~ 0 dBm at six targeted frequencies. Even at the input power of –20 dBm, the return loss is less than –7 dB at 2.1 GHz and 2.6 GHz, and less than –10 dB at the other four frequencies, indicating the proposed rectifier working well over a wide power range. Furthermore, we revealed the impact of the input power level on the RF-DC efficiency and output voltage with respect to the single-tone signal (Fig. 8(f)). As shown in Fig. 8(f), with an increase in the input power level, the RF-DC conversion efficiency and output DC voltage gradually increased in the six designated frequency bands. However, when the input RF power exceeded the threshold values (1 dBm @ 1.8 GHz, 4 dBm @ 2.1 GHz, 3 dBm @ 2.6 GHz, 2 dBm @ 3.5 GHz, 4 dBm @ 4.9 GHz, and 4 dBm @ 5.8 GHz), the output DC voltage saturated owing to the voltage across the Schottky diode exceeding the reverse breakdown voltage, which led to the decay of the efficiency (Fig. 8(f)). Therefore, there is only one peak that can be seen, which is the breakdown power of diode.

Furthermore, considering the advantage of single-diode rectification in multi-tone signal reception, the simulated conversion efficiencies of the proposed rectifier for the three-and six-tone input signals are depicted in Fig. 8(g). With regards to the three-tone signal from port 1 (3.5 GHz + 4.9 GHz + 5.8 GHz), the total efficiency reached 17.2% at the input power level of −20 dBm, which is higher than those of the corresponding single-tone inputs (10.6% @ 3.5 GHz, 8.6% @ 4.9 GHz, and 5% @ 5.8 GHz). A similar phenomenon was observed at port 2. When the per-tone input RF power was fixed at −20 dBm, the introduction of a three-tone signal (with an efficiency of 27% for 1.8 GHz + 2.1 GHz + 2.6 GHz) significantly improved the RF-DC conversion efficiency compared with a single-tone signal (21.6% at 1.8 GHz, 14.7% at 2.1 GHz, and 14% at 2.6 GHz) by more than 13%. Particularly, once a six-tone signal entered our rectifier, the overall efficiency (27% @ −20 dBm, 43% @ −10 dBm) was much higher than that of a single-tone signal at 5.8 GHz (5% @ −20 dBm, 23% @ −10 dBm) with the same input power level, and the maximum enhancement reached 22%, thus resulting in improvement of the RF energy utilization.

It is worth noting that the power loss of RF components and the path loss during RF propagation are inherently related to frequency. As a result, the RF power density for 5G bands may be comparatively lower than that of other bands. Guided by this observation, we've tailored our rectifier to perform optimally at lower power levels within higher frequency bands. Specifically, our rectifier has been honed for –20 dBm and –25 dBm within the 5G and sub-6 GHz bands (2.6 GHz, 3.5 GHz, and 4.9 GHz), as illustrated in Figs. 8(h-i). When juxtaposed with a rectifier optimized for –10 dBm, those refined for –20 dBm and –25 dBm exhibit marginally superior RF-DC efficiency at their respective input power levels. Turning to the conversion efficiency across diverse bands, diode loss stands out as a significant impediment to achieving optimal efficiency, especially at lower input power levels. To address this challenge, a promising approach may involve selecting cutting-edge, low-loss diodes or exploring higher power RF sources for harvesting. For instance, the EIRP for the sub-6 GHz band has been augmented to 53 dBm, a notable increase from the 36 dBm ceiling set for the 2.4 GHz band.

To verify our design, a prototype was printed on a low-cost F4B substrate with a relative permittivity of 2.2, loss tangent of 0.001, and thickness of 0.787 mm, as shown in Fig. 9(a). The reflection coefficient of the rectifier was evaluated using a vector network analyzer (VNA, Agilent E5072A). The measured results at the three different input power levels are presented in Fig. 9(b). Despite the minor variations observed for S_{11} and S_{22}, the measured results shown in Fig. 9(b) are consistent with the simulated results presented in Fig. 8(a). Furthermore, Fig. 9(c) illustrates the measured results of S_{12} at different input power levels, which exhibited a magnitude of less than −20 dB within the frequency range of 1.5 GHz to 6 GHz. These results indicate that the RF power input from one port cannot slip away from the other port.

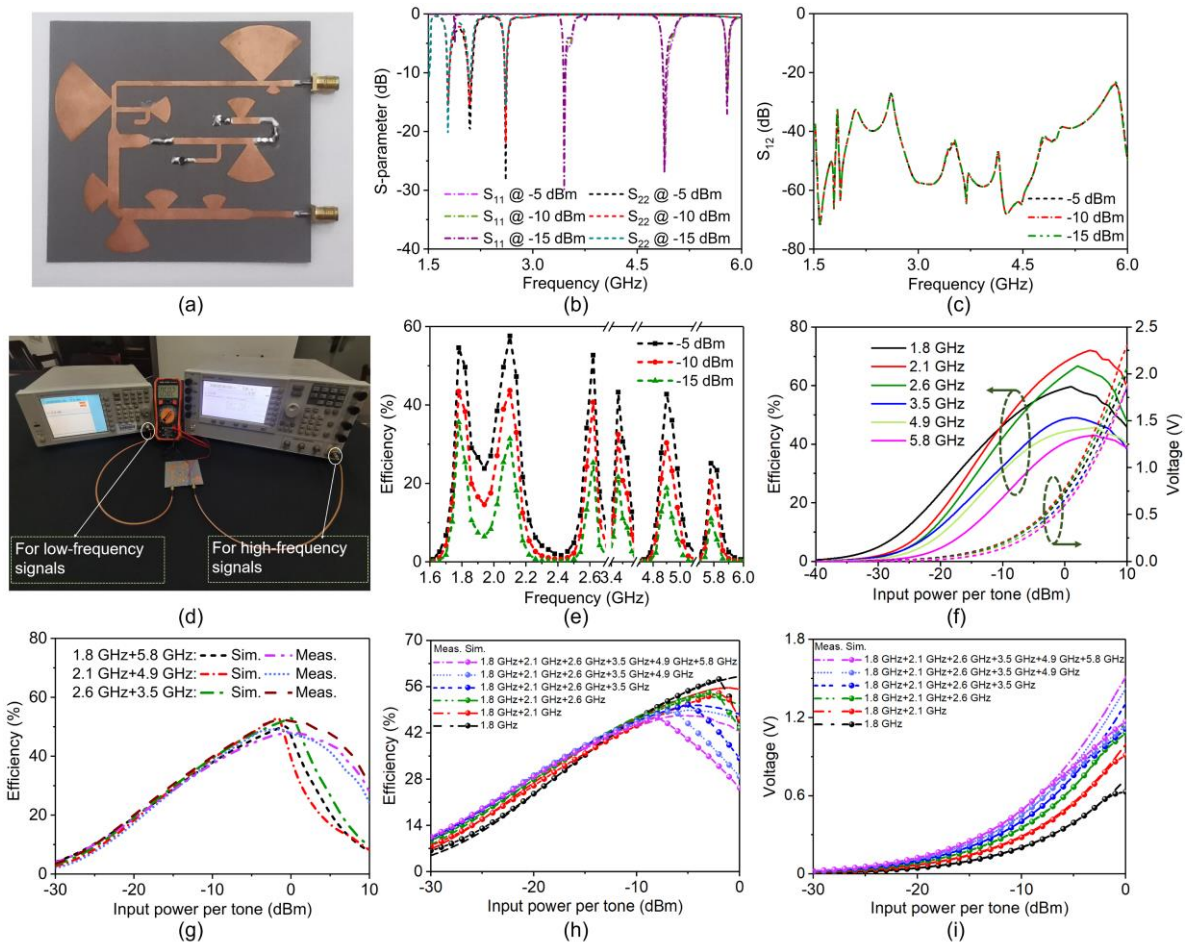

Fig. 9. (a) Photograph of the proposed rectifier. (b) Measured reflection coefficient and (c) S_{12} of the proposed rectifier at different input power levels. (d) Efficiency measurement setup for single-tone and dual-tone signals. (e) Measured RF-DC conversion efficiency of the proposed rectifier versus frequency with different input powers. (f) Measured RF-DC conversion efficiency and output voltage of the proposed rectifier versus input power level at six frequencies. (g) Simulated and measured RF-DC conversion efficiency of the proposed rectifier versus input power level for double-tone input signal. Simulated and measured RF-DC conversion efficiency (h) and output voltage (i) of the proposed rectifier versus input power level for multi-tone input signal. The load resistance is 900 Ω.

Next, to measure the RF-DC conversion efficiency of the proposed rectifier, several RF signal generators (Agilent N9310A, and Keysight E8267D) were used to provide the needed RF signal and power, and a voltmeter was used to measure the voltage across the load. The RF-DC conversion efficiency is obtained using the following equation.

$$\text{Efficiency} = V_{out}^2 / (R \times P_{in}), \tag{9}$$

where R is the optimal load resistance of the rectifier (900 Ω); P_{in} is the input power provided by the signal generators; and V_{out} is the voltage across the load resistance. The measured RF-DC conversion efficiency as a function of frequency is shown in Fig. 9(e) at three input power levels for the load resistance of 900 Ω. Evidently, the rectifier achieved high RF-DC conversion efficiency at the six frequency bands (43.3% @ 1.8 GHz, 43.5% @ 2.1 GHz, 40.8% @ 2.6 GHz, 32% @ 3.5 GHz, 30% @ 4.9 GHz, and 21% @ 5.8 GHz at –10 dBm). Additionally, the measured RF-DC efficiency and output DC voltage varied with the input power at the six frequency bands, as shown in Fig. 9(f). The measured efficiency and voltage were slightly lower than the simulated values (Fig. 8(f)) because of the inaccuracy of the nonlinear model of the diode. However, in contrast to the simulation results shown in Fig. 8(f), the output voltage depicted in Fig. 9(f) continued to increase even after the diode was penetrated. This phenomenon can be attributed to the nonlinear I-V curve of the rectifying diode. Unlike a constant straight line, the reverse voltage increased slightly as the reverse current became indefinite. Furthermore, Figs. 9(e) and 9(f) demonstrate that the max efficiency was different because the proposed rectifier cannot force the diode to operate in a saturated manner at –5 dBm owing to the breakdown voltage of the diode (SMS7630). Consequently, the efficiency further improved as the input RF power increased.

In addition, the RF-DC conversion efficiency of the proposed rectifier under the dual-tone conditions (1.8 GHz + 5.8 GHz, 2.1 GHz + 4.9 GHz, and 2.6 GHz + 3.5 GHz) also has been measured at different input power levels. The input dual-tone signal is carefully selected, of which one tone has high efficiency while the conversion efficiency of the other one is relatively low. As shown in Fig. 9(g), the measured results are consistent with the simulated ones at an input power of less than approximately 0 dBm. When the input power is beyond 0 dBm, the obvious differences can be attributed to the nonlinear I-V curve of the rectifying diode. Unlike a constant straight line, the reverse voltage increased slightly as the reverse current

TABLE I
COMPARISON OF THE PROPOSED RECTIFIER AND RELATED DESIGN

Ref.	Number of bands	Frequency (GHz)	Efficiency of the rectifier for the single-tone signal at −10 dBm	Number of RF signals rectified by one rectifying network*	Measured DC output power at –10 dBm for multi-tone signals	Size (cm^2)	Technology
[34]	5	0.55/0.75/0.98/1.85/2.3	47%/42%/51%/35%/37%	2	NR	3.5 × 4.5	Multiple RF chains with DC combining
[31]	4	0.9/1.8/2.45/5.8	12%/18%/10%/5%	4	NR	NR	Single RF chain
[42]	4	0.84/1.86/2.1/2.45	20%/15%/23%/8%	1	NR	10 × 10	Multiple RF chains with DC combining
[37]	4	0.9/1.75/2.1/2.6	47%/35%/27%/25%	1	–11.1 dBm	3.5 × 3	Multiple RF chains with DC combining
[44]	4	0.85/1.81/2.18/2.4	35%/31%/30%/26%	2	–8.54	NR	Single RF chain
[45]	4	0.92/1.84/2.12/2.24	NR	1	NR	3.2 × 3.5	Multiple RF chains with DC combining
[36]	3	1.85/2.1/2.45	42%/36%/35%	1	–9.1 dBm	10 × 12	Multiple RF chains with DC combining
[43]	4	1.3/1.7/2.4/3.6	22%/16%/4%/2%	4	–11.14 dBm	5.1 × 8.8	Single RF chain
[35]	7	1.84/2.04/2.36/2.54/3.3/4.76/5.8	44.4%/43.9%/45.5%/43.4%/36.1%/32.4%/28.3%	3	NR	5.2 × 4.2	Multiple RF chains with DC combining
This work	**6**	**1.8/2.1/2.6/3.5/4.9/5.8**	**43.3%/43.5%/40.8%/32%/30%/21%**	**6**	**–5.78 dBm**	**9 × 8**	**Dual-port single-branch rectifier with the RNCIE strategy**

*The advantage of having more numbers of RF signal rectified by a single rectifying network or diode is that the total structure can be simplified and the multitone signal can enhance the overall RF-DC efficiency. NR: Not Reported.

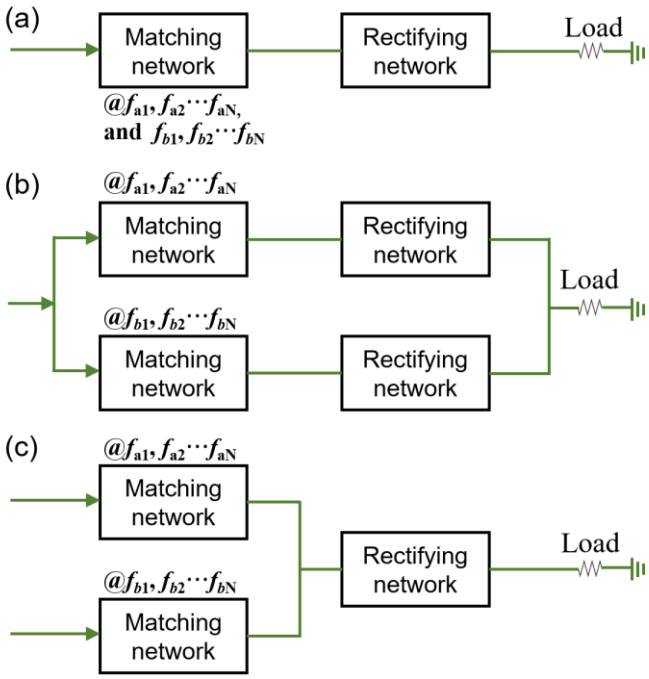

Fig. 10. (a) Single RF chain. (b) Multiple RF chains with DC combining. (c) Proposed rectifier.

became indefinite. The overall efficiency of the dual-tone cases (38% @ 1.8 GHz + 5.8 GHz, 39% @ 2.1 GHz + 4.9 GHz, and 39% @ 2.6 GHz + 3.5 GHz) at −10 dBm per tones are slightly lower than that of same-powered high efficiency parts (43.3% @ 1.8 GHz, 43.5% @ 2.1 GHz, 40.8% @ 2.6 GHz), while are much higher than that of the low efficiency parts (32% @ 3.5 GHz, 30% @ 4.9 GHz, 21% @ 5.8 GHz), directly proving that the proposed rectifier can improve the overall utilization of RF energy. This feature can be further enhanced once the per tones input power is set to −20 dBm due to the relatively low single tone efficiency (21.5% @ 1.8 GHz, 14.2% @ 2.1 GHz, 11.9% @ 2.6 GHz, 10.2% @ 3.5 GHz, 7.6% @ 4.9 GHz, 4.5% @ 5.8 GHz). The corresponding dual-tone efficiency can reach 18.7% @ 1.8 GHz + 5.8 GHz, 17.2% @ 2.1 GHz + 4.9 GHz, and 20% @ 2.6 GHz + 3.5 GHz, which is higher than their single-tone part and results the significant improvement of the overall RF-DC conversion efficiency.

To evaluate the performance of the multi-tone input, both the simulated and measured RF-DC conversion efficiency, and output voltage of the proposed rectifier versus the input power level for the multi-tone input signal are provided in Figs. 9(h) and 9(i). Evidently from Fig. 9(h), the RF-DC efficiency increased as the input power increased and then dropped sharply, as in the single-tone signal cases shown in Fig. 9(f). Furthermore, with an increase in the number of frequency bands, the total generated voltage output (Fig. 9(i)) gradually improved because of the enhanced total RF energy. To further uncover the performance advantage of our design for multi-tone signal cases, the average conversion efficiency of the rectifier is defined as:

$$\text{Efficiency}_{average} = \left(\sum_{i=1}^{k} Eff(f_i)\right)/k, \qquad (10)$$

where Eff(f_i) denotes the single-tone conversion efficiency at the input frequency f_i. Evidently from Fig. 9(h), the realized conversion efficiencies of the rectifier (47.5% @ 1.8 GHz + 2.1 GHz, 46.8% @ 1.8 GHz + 2.1 GHz + 2.6 GHz, 45.6% @ 1.8 GHz + 2.1 GHz + 2.6 GHz + 3.5 GHz, 45.1% @ 1.8 GHz + 2.1 GHz + 2.6 GHz + 3.5 GHz + 4.9 GHz, 44% @ 1.8 GHz + 2.1 GHz + 2.6 GHz + 3.5 GHz + 4.9 GHz + 5.8 GHz) working under the multi-tone input condition were larger than their average ones (46.6% @ 1.8 GHz + 2.1 GHz, 45.1% @ 1.8 GHz + 2.1 GHz + 2.6 GHz, 41.4% @ 1.8 GHz + 2.1 GHz + 2.6 GHz + 3.5 GHz, 39.5% @ 1.8 GHz + 2.1 GHz + 2.6 GHz + 3.5 GHz + 4.9 GHz, 36.4% @ 1.8 GHz + 2.1 GHz + 2.6 GHz + 3.5 GHz

+ 4.9 GHz + 5.8 GHz) at −10 dBm. Particularly, the conversion efficiency (28.8%) under the six-tone input condition was 15.5% higher than the average efficiency (13.3%) at the input power of −20 dBm, thus demonstrating the unique superiority compared with other multiple RF chain designs.

Finally, a comparison between our rectifier design and some recent rectifier designs is provided in Table I. In comparison to the single RF chain topology (Fig. 10(a)) and multiple RF chains topology (Fig. 10(b)), our design introduces a new topology as depicted in Fig. 10(c). This new topology allows for improved RF-DC efficiency and operation frequency bands. In the case of a single branch multi-band rectifier, each frequency signal passes through the entire matching network, resulting in a fixed insertion loss for signals at different bands. However, in our proposed case, the matching network is multi-band and frequency selective. This allows each signal to pass through a unique branch of a single/multi-band with lower insertion loss, unlike the single branch scenarios. Evidently, with help of the proposed topology, our design is better than those in [31, 34, 36, 37, 42–45] in terms of the operation frequency, RF-DC conversion efficiency with respect to the single-tone signal, and measured DC output power with respect to the multi-tone signal.

Although the rectifier in [35] can operate in seven frequency bands, the design process becomes more complex due to impedance coupling between each RF chain. In contrast, our proposed topology introduces a corresponding design method called the three-port matching network, which helps reduce the coupling. This allows the rectifier design to be divided into different network designs, including the rectifying network, filter-branch, and matching-branch. As a result, our proposed topology offers a time and resource-saving solution. Furthermore, our design is the only one (as presented in Table I) that can simultaneously convert RF power into DC energy using a one-diode shared rectifying network across all six frequency bands. This unique capability allows for significant improvements in RF-DC efficiency under multi-tone input conditions, thus resulting in the rectifier achieving the highest DC output among the compared designs. Therefore, the proposed rectifier is no doubt a very good candidate for RF energy harvesting in numerous practical applications.

V. Conclusion

In this study, we successfully designed and demonstrated a dual-port six-band rectifier based on the proposed RNCIE design strategy, which involves the extraction of common elements. Our approach offers several advantages over the time-consuming global optimization method for designing complex multi-band rectifiers (more than three bands), such as the clearly defined functional zones for decomposing common problems like mutual coupling between RF chains and the extra insertion loss caused by complex matching networks. The experimental results obtained from our prototype demonstrated that the proposed rectifier exhibits high and competitive RF-DC conversion efficiency across multiple frequency bands, further validating the effectiveness of our design strategy. In conclusion, we believe that this design strategy has significant potential for future high-performance rectifier design.

References

[1] J.-S. Park, Y.-S. Choi, and W.-S. Lee, "Design of miniaturized incident angle-insensitive 2.45 GHz RF-based energy harvesting system for IoT Applications," *IEEE Trans. Antennas and Propag.*, vol. 70, no. 5, pp. 3781-3788, Feb. 2022.

[2] Z. Li, J. -W. Zhang, Y. -C. Wang, D. -P. He and C. Zhang, "Two-port five-band rectenna for ultralow ambient RF energy harvesting," *IEEE Antennas and Wireless Propag*. Letters, vol. 22, no. 8, pp. 1972-1976, Aug. 2023.

[3] K. Shafique et al., "Energy harvesting using a low-cost rectenna for Internet of Things (IoT) applications," *IEEE Access*, vol. 6, pp. 30932-30941, Feb. 2018.

[4] N. Mirzababaee, F. Geran, and S. Mohanna, "A radio frequency energy harvesting rectenna for GSM, LTE, WLAN, and WiMAX," *Int. J. RF Microw. Comput.*, vol. 55, no. 2, pp. 35–42, Mar. 2021.

[5] M. Cansiz, D. Altinel, and G. K. Kurt, "Efficiency in RF energy harvesting systems: A comprehensive review," *Energy*, vol. 174, pp. 292-309, Mar. 2019.

[6] S. Roy, J.-J. Tiang, M. B. Roslee, M. T. Ahmed, and M. A. P. Mahmud, "A quad-band stacked hybrid ambient RF-solar energy harvester with higher RF-to-DC rectification efficiency," *IEEE Access*, vol. 9, pp. 39303-39321, Feb. 2021.

[7] L. Lu, M. Yi, and X. Liu, "Energy-efficient firing modes of chay neuron model in different bursting kinetics," *Science China Techn. Sciences*, vol. 65, no. 8, pp. 1661-1674, Aug. 2022.

[8] J. Antonio Estrada et al., "RF-harvesting tightly coupled rectenna array tee-shirt with greater than octave bandwidth," *IEEE Trans. Microw. Theory Techn.*, vol. 68, no. 9, pp. 3908-3919, Mar. 2020.

[9] M. Aboualalaa, I. Mansour, and R. K. Pokharel, "Energy harvesting rectenna using high-gain triple-band antenna for powering Internet-of-Things (IoT) devices in a smart office," *IEEE Trans. Instrum. and Meas.*, vol. 72, pp. 1-12, Feb. 2023.

[10] T. Paing, J. Shin, R. Zane, and Z. Popovic, "Resistor emulation approach to low-power RF energy harvesting," *IEEE Trans. Power Electron.*, vol. 23, no. 3, pp. 1494-1501, Aug. 2008.

[11] V. Marian, B. Allard, C. Vollaire, and J. Verdier, "Strategy for microwave energy harvesting from ambient field or a feeding source," *IEEE Trans. Power Electron.*, vol. 27, no. 11, pp. 4481-4491, Mar. 2012.

[12] P. Lu, C. Song, F. Cheng, B. Zhang, and K. Huang, "A self-biased adaptive reconfigurable rectenna for microwave power transmission," *IEEE Trans. Power Electron.*, vol. 35, no. 8, pp. 7749-7754, Feb. 2020.

[13] Z. He, J. Lan, and C. Liu, "Compact rectifiers with ultra-wide input power range based on nonlinear impedance characteristics of schottky diodes," *IEEE Trans. Power Electron.*, vol. 36, no. 7, pp. 7407-7411, Aug. 2021.

[14] Y. Han, O. Leitermann, D. A. Jackson, J. M. Rivas, and D. J. Perreault, "Resistance compression networks for radio-frequency power conversion," *IEEE Trans. Power Electron.*, vol. 22, no. 1, pp. 41-53, Feb. 2007.

[15] K. Dang et al., "A 5.8-GHz high-power and high-efficiency rectifier circuit with lateral GaN schottky diode for wireless power transfer," *IEEE Trans. Power Electron.*, vol. 35, no. 3, pp. 2247-2252, Mar. 2020.

[16] P. Lu, C. Song, and K. M. Huang, "A compact rectenna design with wide input power range for wireless power transfer," *IEEE Trans. Power Electron.*, vol. 35, no. 7, pp. 6705-6710, Sep. 2020.

[17] P. Lu, X.-S. Yang, J.-L. Li, and B.-Z. Wang, "A compact frequency reconfigurable rectenna for 5.2- and 5.8-GHz wireless power transmission," *IEEE Trans. Power Electron.*, vol. 30, no. 11, pp. 6006-6010, Mar. 2015.

[18] D. Potti, G. N. A. Mohammed, K. Savarimuthu, S. Narendhiran, and G. Rajamanickam, "An ultra-wideband rectenna using optically transparent Vivaldi antenna for radio frequency energy harvesting," *Intern. Journal of RF and Micro. Computer-Aided Engin.*, vol. 30, no. 10, Nov. 2020.

[19] B. Patrick Motjolopane and R. van Zyl, "A review of rectenna models for electromagnetic energy harvesting," *Journal of Engin., Design and Techn.*, vol. 7, no. 3, pp. 282-292, Nov. 2009.

[20] X. Zhang et al., "Two-dimensional MoS2-enabled flexible rectenna for Wi-Fi-band wireless energy harvesting," *Nature*, vol. 566, no. 7744, pp. 368-372, Feb. 2019.

[21] W. Lin and R. W. Ziolkowski, "Electrically small huygens CP rectenna with a driven loop element maximizes its wireless power transfer

efficiency," *IEEE Trans. Antennas and Propag.*, vol. 68, no. 1, pp. 540-545, Sep. 2020.

[22] M. Kumar, S. Kumar, A. S. Bhadauria, and A. Sharma, "A planar integrated rectenna array with 3-D-spherical DC coverage for orientation-tolerant wireless-power-transfer-enabled IoT sensor nodes," *IEEE Trans. Antennas and Propag.*, vol. 71, no. 2, pp. 1285-1294, Feb. 2023.

[23] J. A. Hagerty, F. B. Helmbrecht, W. H. McCalpin, R. Zane, and Z. B. Popovic, "Recycling ambient microwave energy with broad-band rectenna arrays," *IEEE Trans. Microw. Theory Techn.*, vol. 52, no. 3, pp. 1014-1024, Feb. 2004.

[24] M. Varasteh, B. Rassouli, and B. Clerckx, "On capacity-achieving distributions for complex AWGN channels under nonlinear power constraints and their applications to SWIPT," *IEEE Trans. Inform. Theory*, vol. 66, no. 10, pp. 6488-6508, Aug. 2020.

[25] G. Verma and V. Sharma, "A novel RF energy harvester for event-based environmental monitoring in wireless sensor networks," *IEEE Internet of Things Journal*, vol. 9, no. 5, pp. 3189-3203, Sep. 2022.

[26] C. Song et al., "Matching network elimination in broadband rectennas for high-efficiency wireless power transfer and energy harvesting," I*EEE Trans. Ind. Electron.*, vol. 64, no. 5, pp. 3950-3961, Nov. 2017.

[27] S. F. Bo, J.-H. Ou, Y. Dong, S.-W. Dong, and X. Y. Zhang, "All-polarized wideband rectenna with enhanced efficiency within wide input power and load ranges," *IEEE Trans. Ind. Electron.*, vol. 69, no. 7, pp. 7470-7480, Nov. 2022.

[28] F. Bolos, J. Blanco, A. Collado, and A. Georgiadis, "RF energy harvesting from multi-tone and digitally modulated signals," *IEEE Trans. Microw. Theory Techn.*, vol. 64, no. 6, pp. 1918-1927, Feb. 2016.

[29] S.-B. Liu, F.-S. Zhang, M. Boyuan, S.-P. Gao, and Y.-X. Guo, "Multiband dual-polarized hybrid antenna with complementary beam for simultaneous RF energy harvesting and WPT," *IEEE Trans. Antennas and Propag.*, vol. 70, no. 9, pp. 8485-8495, Aug. 2022.

[30] S. Nagaveni, S. S. Regulagadda, and A. Dutta, "A stage-stage dead-band compensated multiband RF energy harvester for sensor nodes," *IEEE Sensors Journal*, pp. 1-1, Aug. 2023.

[31] C. Wang, J. Zhang, S. Bai, D. Chang, and L. Duan, "A multi-band compact flexible energy collector for wearable or portable IoT devices," *IEEE Antennas and Wireless Propag*. Letters, pp. 1-5, Mar. 2023.

[32] S. Roy, R. J. -J. Tiang, M. B. Roslee, M. T. Ahmed and M. A. P. Mahmud, "Quad-band multiport rectenna for RF energy harvesting in ambient environment," *IEEE Access*, vol. 9, pp. 77464-77481, May 2021.

[33] B. Alzahrani and W. Ejaz, "Resource management for cognitive IoT systems with RF energy harvesting in smart cities," *IEEE Access*, vol. 6, pp. 62717-62727, Mar. 2018.

[34] C. Song et al., "A novel six-band dual CP rectenna using improved impedance matching technique for ambient RF energy harvesting," *IEEE Trans. Antennas and Propag.*, vol. 64, no. 7, pp. 3160-3171, Nov. 2016.

[35] Y. Wang et al., "Efficiency enhanced seven-band omnidirectional rectenna for RF energy harvesting," *IEEE Trans. Antennas and Propag.*, vol. 70, no. 9, pp. 8473-8484, Dec. 2022.

[36] M. Q. Dinh and M. Thuy Le, "Triplexer-based multiband rectenna for RF energy harvesting from 3G/4G and Wi-Fi," *IEEE Micro. and Wire. Components Lett.*, vol. 31, no. 9, pp. 1094-1097, Feb. 2021.

[37] V. Palazzi et al., "A novel ultra-lightweight multiband rectenna on paper for RF energy harvesting in the next generation LTE bands," *IEEE Trans. Microw. Theory Techn.*, vol. 66, no. 1, pp. 366-379, Dec. 2018.

[38] Surface Mount Mixer and Detector Schottky Diodes, Data Sheet, skyworks Solutions, Woburn, MA, USA, 2013.

[39] S. Cao, Y. Jiao, Z. Zhang, "Applications of generalized cascade scattering matrix on the microwave circuits and antenna arrays," *Intern. Journal of Antennas and Propag.*, vol. 10, no 12, pp. 12, Apr. 2015.

[40] W. Duk-Jae, L. Taek-Kyung, L. Jae-Wook, P. Cheol-Sig, and C. Won-Kyu, "Novel U-slot and V-slot DGSs for bandstop filter with improved Q factor," *IEEE Trans. Microw. Theory Techn.*, vol. 54, no. 6, pp. 2840-2847, Jun. 2006.

[41] E. J. Naglich and A. C. Guyette, "Reflection-mode bandstop filters with minimum through-line length," *IEEE Trans. Microw. Theory Techn.*, vol. 63, no. 10, pp. 3479-3486, Oct. 2015.

[42] H. S. Vu, N. Nguyen, N. Ha-Van, C. Seo and M. Thuy Le, "Multiband ambient RF energy harvesting for autonomous IoT devices," *IEEE Micro. and Wire. Components Lett.*, vol. 30, no. 12, pp. 1189-1192, Dec. 2020.

[43] C. -Y. Hsu, S. -C. Lin and Z. -M. Tsai, "Quadband rectifier using resonant matching networks for enhanced harvesting capability," *IEEE Micro. and Wire. Components Lett.*, vol. 27, no. 7, pp. 669-671, Jul. 2017.

[44] S. Roy, J. J. Tiang, M. B. Roslee, M. T. Ahmed, A. Z. Kouzani, and M. A. P. Mahmud, "Quad-band rectenna for ambient radio frequency (RF) energy harvesting," *Sensors*, vol. 21, no. 23, pp. 1189-1192, Nov. 2021.

[45] S. Roy, J. J. Tiang, M. B. Roslee, M. T. Ahmed, A. Z. Kouzani, and M. A. P. Mahmud, "Design of a highly efficient wideband multi-frequency ambient RF energy harvester," *Sensors*, vol. 22, no. 2, pp. 41-53, Jan. 2022.